nature medicine

ARTICLES

https://doi.org/10.1038/s41591-018-0206-4

Neurogenetic contributions to amyloid beta and tau spreading in the human cortex

Jorge Sepulcre[1,2]*, Michel J. Grothe[3], Federico d'Oleire Uquillas[4], Laura Ortiz-Terán[1], Ibai Diez[1,5], Hyun-Sik Yang[4,6], Heidi I. L. Jacobs[1], Bernard J. Hanseeuw[1,2,7], Quanzheng Li[1], Georges El-Fakhri[1], Reisa A. Sperling[2,4,6] and Keith A. Johnson[1,4,6]

Tau and amyloid beta (Aβ) proteins accumulate along neuronal circuits in Alzheimer's disease. Unraveling the genetic background for the regional vulnerability of these proteinopathies can help in understanding the mechanisms of pathology progression. To that end, we developed a novel graph theory approach and used it to investigate the intersection of longitudinal Aβ and tau positron emission tomography imaging of healthy adult individuals and the genetic transcriptome of the Allen Human Brain Atlas. We identified distinctive pathways for tau and Aβ accumulation, of which the tau pathways correlated with cognitive levels. We found that tau propagation and Aβ propagation patterns were associated with a common genetic profile related to lipid metabolism, in which *APOE* played a central role, whereas the tau-specific genetic profile was classified as 'axon related' and the Aβ profile as 'dendrite related'. This study reveals distinct genetic profiles that may confer vulnerability to tau and Aβ in vivo propagation in the human brain.

Alzheimer's disease (AD) is characterized by the abnormal accumulation of tau and Aβ proteins, a process that is known to affect specific neuronal systems. In fact, it has been consistently shown that both of these pathological hallmarks of AD affect specific large-scale circuits, whereas other circuits remain spared or become disrupted later in the disease[1–5]. Moreover, genetic population studies have shown that AD can be genetically determined, such as in familial forms of AD characterized by *APP* (encoding amyloid precursor protein), *PSEN1* (encoding presenilin 1) or *PSEN2* mutations, or genetically predisposed, such as in late-onset sporadic AD, which is highly associated with apolipoprotein E (*APOE*) ε4 allele positivity (and, to a lesser extent, to polygenic associations of ~20 genes thus far described in the literature[6–11]). However, it is still unknown whether and how these genetic factors confer vulnerability to the distinct spread of AD pathology across specific neuronal circuits in the aging brain. Several reasons can be speculated for this neglect. Until now, we have lacked the analytical tools to determine in vivo longitudinal propagation patterns of tau and Aβ deposits in the human brain. This has precluded the detection of pathways related to the progression of AD pathology in cerebral tissue, as well as the investigation of genetic features potentially related with hypothesized pathways. Second, until the advent of microarray data covering the protein-coding transcriptome of the entire human cerebral tissue (Allen Human Brain Atlas (AHBA))[12,13], we have lacked high-spatial-resolution data for investigating gene expression levels associated with cortical anatomy. Third, we have lacked research approaches for combining findings from in vivo tau and Aβ propagation topologies with genetic profiles of cerebral circuits. Overall, the characterization of the neurogenetic basis of the cortical spreading of AD pathology would provide a critical understanding of how genes interact with AD pathology and neurodegeneration[14].

AD dementia is a major public health challenge and one that poses an even greater threat as the current population ages. Recently, preclinical stages of AD have been a major topic of investigation, motivated by the acknowledgment that the pathophysiological process begins decades before any cognitive decline appears[15]. Thus, studying the pathways in which tau and Aβ spreads early on, as well as studying the genetic underpinnings of the respective spreading pathways, is crucial for advancing diagnostic accuracy as well as for enabling early disease-modifying interventions. Following that rationale, in this study, we hypothesized that specific gene expression profiles in brain tissue sustain the propagation selectivity of AD pathology along specific neuronal systems. To that end, we first focused on the identification of in vivo propagation pathways of tau and Aβ deposits in a longitudinal sample of healthy adult study participants (SP) from the Harvard Aging Brain Study (HABS)[16–19]. We developed graph theory metrics to detect the main cortical routes of pathology progression at the group level using positron emission tomography (PET) imaging, and built a novel staging approach to investigate subject-level pathway profiles of spreading of pathology and their relationship with neuropsychological and cognitive profiles. Last, using the AHBA, we characterized regional gene expression profiles associated with tau and Aβ PET pathology progression patterns across the cerebral cortex to better understand at the neural systems level the vulnerability that AD-related genetic profiles confer on AD pathology progression in the human brain.

Results

Propagation routes from prominent areas of tau and amyloid deposits. Using no-overlapping cross-sectional ($n=69$ HABS healthy adults) and longitudinal ($n=19$ HABS healthy adults)

[1]Gordon Center for Medical Imaging, Department of Radiology, Massachusetts General Hospital, Harvard Medical School, Boston, MA, USA. [2]Athinoula A. Martinos Center for Biomedical Imaging, Department of Radiology, Massachusetts General Hospital, Harvard Medical School, Charlestown, MA, USA. [3]German Center for Neurodegenerative Diseases (DZNE), Rostock, Germany. [4]Department of Neurology, Massachusetts General Hospital, Harvard Medical School, Boston, MA, USA. [5]Neurotechnology Laboratory, Tecnalia Health Department, Derio, Spain. [6]Centre for Alzheimer Research and Treatment, Department of Neurology, Brigham and Women's Hospital, Harvard Medical School, Boston, MA, USA. [7]Department of Neurology, Saint-Luc University Hospital, Institute of Neuroscience, University of Louvain, Brussels, Belgium. *e-mail: sepulcre@nmr.mgh.harvard.edu

data from HABS participants ($n=88$; Supplementary Table 1), we detected distinct propagation pathways for tau and Aβ accumulation. We developed a graph theory approach, named directional graph theory regression (DGTR; Supplementary Fig. 1), to predict at the cross-sectional level and corroborate at the longitudinal level, brain tau and Aβ pathology changes as imaged by in vivo PET imaging in samples of healthy adult individuals. By doing so, the cross-sectional tau findings predicted graph-based connectivity between the temporal region of interest and the anterior and inferior part of the temporal lobe, as well as midline frontal regions, such as the orbitofrontal cortex (Fig. 1a). The longitudinal tau findings not only confirmed anterior and inferior temporal lobe and midline frontal regions as spatiotemporal targets for tau propagation but additionally revealed that these pathways also extend from the temporal lobe into the posterior cingulate cortex (PCC) and precuneus (Fig. 1b). Overall, we found a high spatial association between cross-sectionally predicted and longitudinally observed network propagation of tau (scatter plot in Fig. 1; $r=0.599$). Analogous results were obtained with a replication data set ($n=24$ HABS healthy adults), both with and without partial volume correction (PVC; Supplementary Fig. 2). We also detected propagation pathways of Aβ, in which the PCC was related with distributed regions in the lateral frontoparietal, midline frontal and precuneus regions at the cross-sectional level (Fig. 1c). The longitudinal findings confirmed that Aβ predominantly spreads toward neighboring posterior and lateral parietal lobe regions (Fig. 1d). Analogous to tau propagation, we found a high spatial association between cross-sectionally predicted and longitudinally observed network propagation of Aβ (scatter plot in Fig. 1; $r=0.623$). Similar results were obtained with the replication data set, both with and without PVC (Supplementary Fig. 2).

Hubs of pathology propagation of tau and amyloid. Next, we detected brain regions where a disproportionate number of propagation routes converged in our longitudinal sample, either as out-degree hubs (regions for which the signal in time 1 explained the signal of many other regions in time 2 (see the small-network diagram in Fig. 2)) or in-degree hubs (regions in which the signal in time 2 is explained by the signal of many other regions in time 1 (see the small-network diagram in Fig. 2)) of pathology. On the one hand, we found that tau out-degree hubs were mostly located in the medial temporal lobe, including the parahippocampus and the inferior temporal neocortex (top-left cortical maps in Fig. 2a), whereas tau in-degree hubs involved the mid-cingulate cortex/PCC and some frontal dorsal areas (bottom-left cortical maps in Fig. 2a). The aggregation display showed that tau out-degree hubs and in-degree hubs were distantly located without overlap (cortical overlap map in Fig. 2a). On the other hand, we found that Aβ out-degree hubs were mostly found in angular and supramarginal gyri, the PCC and the mid/superior frontal regions (top-right cortical maps in Fig. 2b), whereas Aβ in-degree hubs were located in the precuneus, left inferior and superior parietal cortex and the confluence between the superior frontal gyrus and the supplementary motor area (bottom-right cortical maps in Fig. 2b). The aggregation display showed that Aβ out-degree hubs and in-degree hubs display a high degree of overlap in the angular gyrus and some degree of overlap at the junction between the PCC and the precuneus (cortical overlap map in Fig. 2b).

Tau and amyloid propagation-based method in individual subjects. Next, we used the main out-degree and in-degree propagation pathways obtained in the DGTR analysis at the group level to characterize individual tau and amyloid deposition profiles in the SP sample ($n=64$; SP with complete neuropsychological assessment), as well as in an additional sample of AD/mild cognitive impairment (MCI) individuals ($n=19$), both from our cross-sectional data (Fig. 3). To build this propagation-based method, we extracted the main tau propagation routes—seven in total: mid-cingulate cortex/PCC, bilateral dorsal frontal, bilateral temporal pole, bilateral medial/inferior temporal—and the main Aβ propagation routes—six in total: PCC, mid/superior frontal, bilateral inferior parietal and lateral temporal—based on the out-degree and in-degree hubs maps (see the arrows in the polar plots of Fig. 3a). Each of these tau and Aβ propagation routes showed significant differences between elderly subjects and AD groups (violin plots in Fig. 3a). Moreover, using this propagation-based approach, we found that lower global cognition and lower memory scores were associated to specific tau pathways in this cross-sectional data, particularly deposits involving the temporal lobe (see the correlation matrix and scatter plots in Fig. 3b), with no associations found for executive functions. Propagation-based analysis of Aβ routes was not associated with any cognitive measure.

Brain colocalization of in vivo propagation patterns and Allen gene expression data. Among the 21 pre-selected genes with known AD risk association, we found that *MAPT* (encoding tau protein; star symbol in Fig. 4a; scatter plot and cortical map in Fig. 4b) reached the highest level of brain colocalization with the imaging propagation map of tau (tau out-degree hubs map plus tau in-degree hubs map; cortical map in Fig. 4b), whereas *CLU* (encoding clusterin protein; star symbol in Fig. 4a; scatter plot and cortical map in Fig. 4d) reached the highest level of brain colocalization with the imaging propagation map of Aβ (Aβ out-degree hubs map plus Aβ in-degree hubs map; cortical map in Fig. 4d). Importantly, *MAPT* ($P=0.006$) and *CLU* ($P=0.018$) were the only genes of our pre-selected genetic set that showed significance when contrasting them against the null hypothesis distribution based on the entire protein-coding transcriptome (Fig. 4c,e). Moreover, *MAPT* and *CLU* gene expression levels were not associated with raw standardized uptake value ratio (SUVR) tau and distribution volume ratio (DVR) Aβ intensity maps from the same sample (Fig. 4f), indicating that the expression of these genes is associated with the regional propagation of tau and Aβ, respectively, and not with SUVR tau or DVR Aβ intensity levels of pathology.

Finally, we further conducted data-driven analyses in addition to the analysis of pre-selected AD risk genes, to identify genes with expression patterns that are spatially correlated with Aβ or tau propagation maps: 354 genes correlated with the tau imaging propagation pattern and 216 genes with the Aβ imaging propagation pattern. Interestingly, 123 genes were correlated with both tau and Aβ imaging propagation patterns (Fig. 4c,e; see these three lists of genes along with their putative functions in Supplementary Tables 3–6).

Interactome and Gene Ontology analyses of imaging genetic profiles. Next, we investigated the genetic interactions and biological functionality of the 123 genes with expression patterns correlated with both tau and Aβ propagation (Fig. 5a). We found that the genetic network of these shared genes displayed a dense organization of interactions in which lipid metabolism annotations were the most relevant neuro-related biological process and cellular component functionality (Fig. 5a; family-wise error (FWE)-corrected $P<0.05$). This interactome analysis showed that lipid metabolism genes—belonging to the common profile of tau and Aβ—interact with other genes such as *APOE*, which exhibit a central role in genetic network relationships (see the network layout and centrality graph in Fig. 5a). Then, we performed further exploratory analysis of interactomes and Gene Ontology of genes with expression patterns correlated specifically with tau (Fig. 5b) or Aβ propagation (Fig. 5c). The network of tau-related genes seemed to yield a dense organization of interactive genes in which neuron and axon organization was the most relevant neuro-related biological process and cellular component functionality (Fig. 5b; FWE-corrected $P<0.05$). For instance, this interactome analysis showed that genes implicated

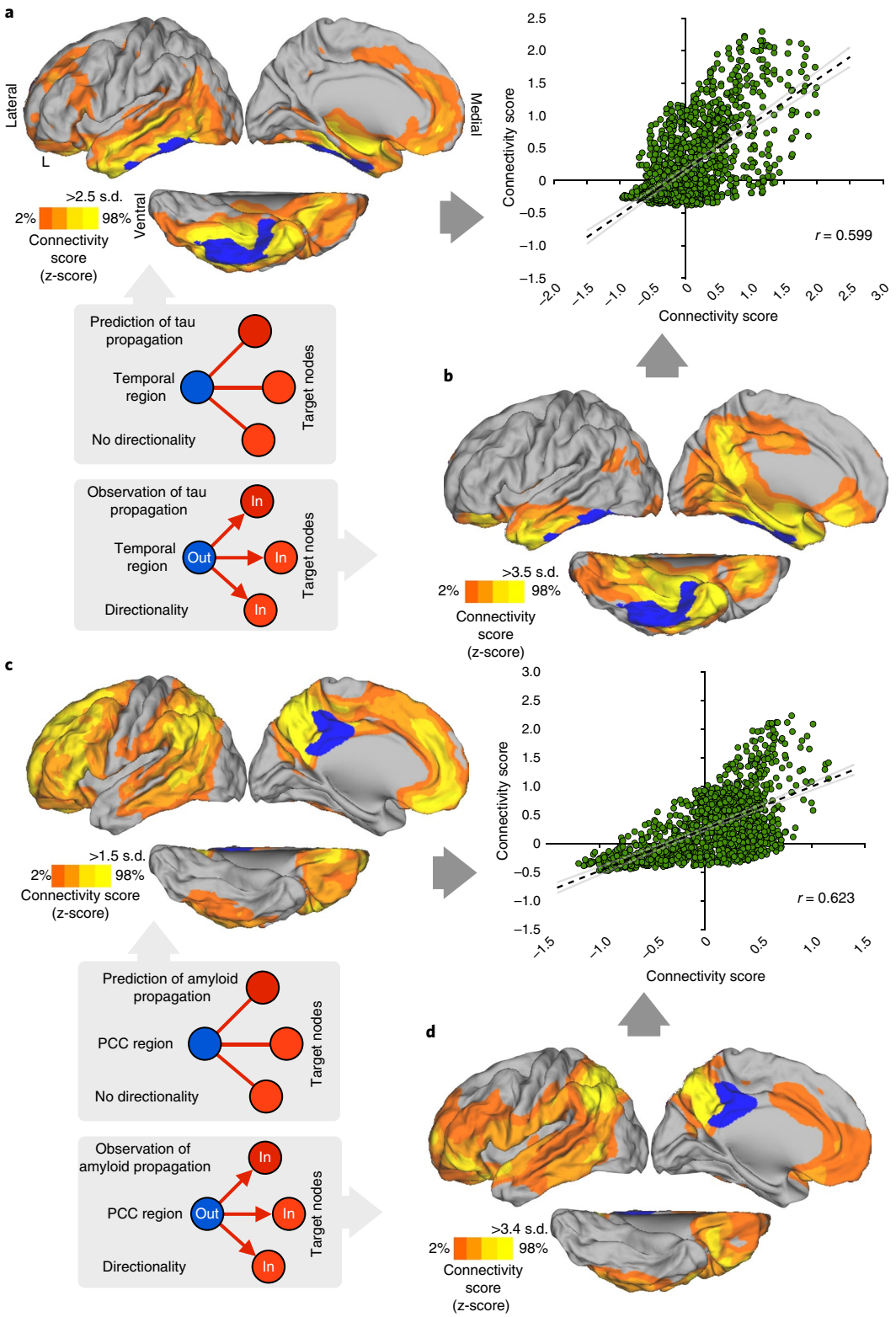

Fig. 1 | Propagation routes from prominent areas of tau and amyloid deposits. a–d, Cortical connectivity maps of a priori selected areas, namely, the inferior temporal cortex for tau (**a**,**b**) and the PCC for Aβ (**c**,**d**), from cross-sectional (**a** and **c**; $n = 69$, HABS healthy adults) and longitudinal (**b** and **d**; $n = 19$ HABS healthy adults) data. Scatter plots of spatial similarity between cross-sectionally predicted and longitudinally observed network connectivity profiles (green dots) are shown. The *x* and *y* axes show the z-scores of the connectivity values. The network diagrams illustrate theoretical examples of seed-based connectivity in cross-sectional (no arrows) and longitudinal (arrows) samples.

in microtubule organization, such as *CNTN2* (top 1), *DPYSL2* (top 3) and *MAP1B* (top 19), displayed a central role in these genetic interactions (see network layout and centrality graph in Fig. 5b). *MAPT* had a less central role in this network and it did not hold a position among the top 25 most central genes (the centrality graph in Fig. 5b). Moreover, we found that *BACE1* (encoding

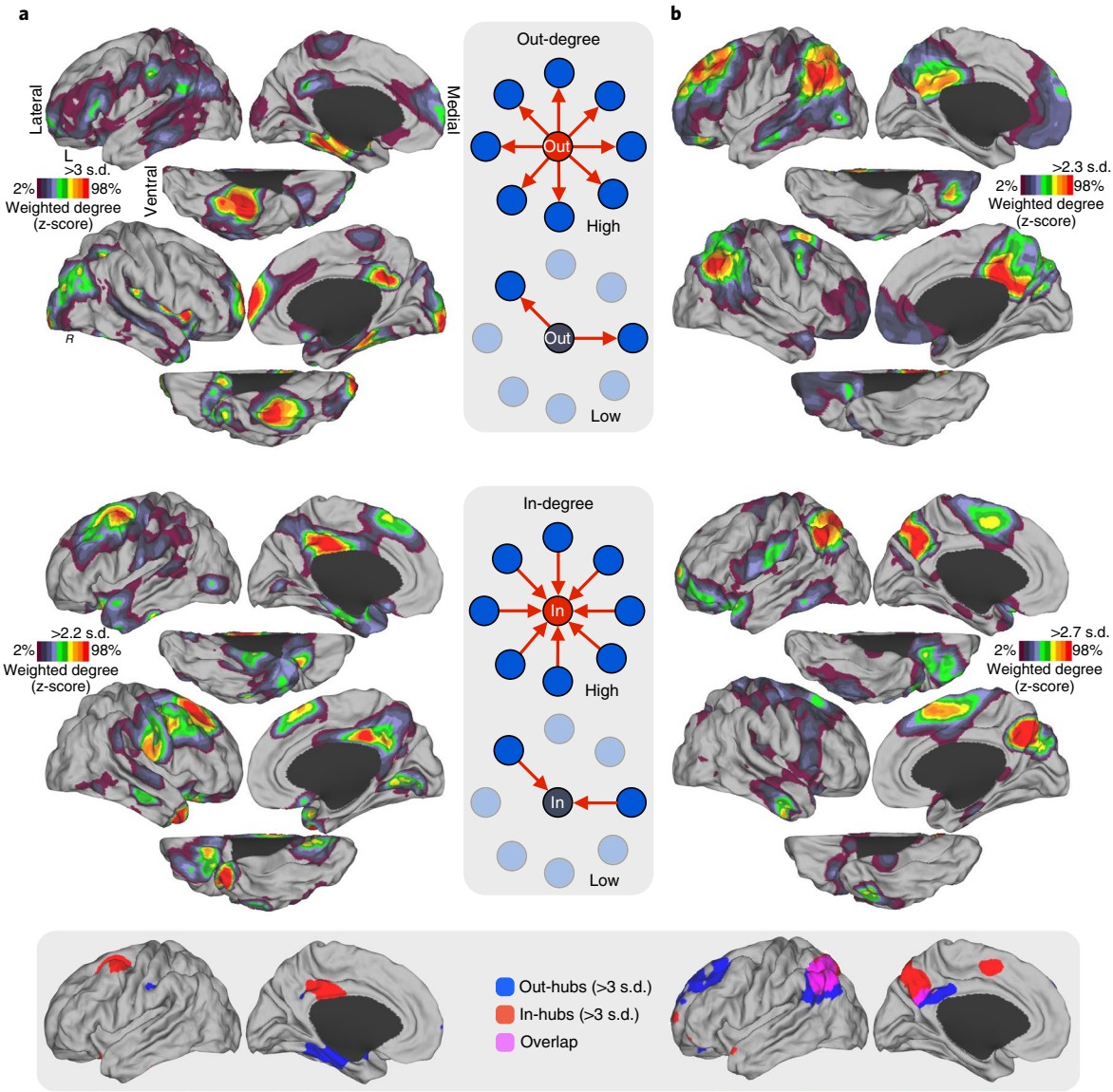

Fig. 2 | Hubs of pathology propagation of tau and amyloid. a,**b**, Cortical maps of longitudinal weighted-degree connectivity (directional relationships) of tau (**a**; out-degree maps in the top left; in-degree maps in the middle left; $n=19$ HABS healthy adults) or Aβ pathways (**b**; out-degree maps in the top right; in-degree maps in the middle right; $n=19$ HABS healthy adults). Network diagrams illustrate high and low theoretical examples of out-degree and in-degree. Overlap maps with an arbitrary threshold of z-score ≥ 3 s.d. across the cortical mantle of tau (bottom left) and Aβ (bottom right) are also presented.

β-secretase 1)—a gene related to the cleaving of APP—was a relevant interacting gene in this genetic network (see the network layout and centrality graph in Fig. 5b). The gene network of Aβ-related genes showed a dense organization of interactions in which dendrite and neuron organization annotations arose as the most relevant neuro-related biological process and cellular component functionality (Fig. 5c; FWE-corrected $P<0.05$). Interestingly, this interactome analysis showed that genes related to transcriptional regulation of APP, such as *APBB1* (top 14) and *CLU* (top 22), interact with protein-coding genes involved in neuronal cytoskeletal organization, such as *TUBA1A* (top 3) or *TUBA4A* (top 16) (see the network layout and centrality graph in Fig. 5c).

Propagation-based staging of tau, Aβ and *APOE* genotype. In Fig. 6a, we summarize the main neuroimaging transcriptomic findings and contextualize them with our PET approach. Based on this framework in which different AD-related genotypes are expected to differently affect the tau and/or Aβ molecular pathways, we predicted that genes involved in both tau and Aβ genetic interactome profiles (the gray area in Fig. 6a) would induce a concomitant tau and Aβ vulnerability. To estimate this assumption, we investigated the propagation-based staging and *APOE* genotyping in SP individuals of our cross-sectional sample for which *APOE* ε4 carrier status was available ($n=68$; 21 *APOE* ε4$^+$ and 47 *APOE* ε4$^-$). We averaged all propagation-based staging scores from Fig. 3 and obtained global scores for individual tau and Aβ burden. Importantly, we found that *APOE* ε4$^+$ participants displayed a linear relationship between tau and Aβ load in the respective propagation pathways, whereas *APOE* ε4$^-$ participants did not show any such association (Fig. 6b).

Discussion

What makes specific neuronal systems vulnerable to the accumulation of AD pathology remains a field of intense research. Recent advances in multitracer PET neuroimaging, particularly those targeting tau and Aβ, as well as advances in genetic biomarker research, have provided new, exciting opportunities for studying AD-specific

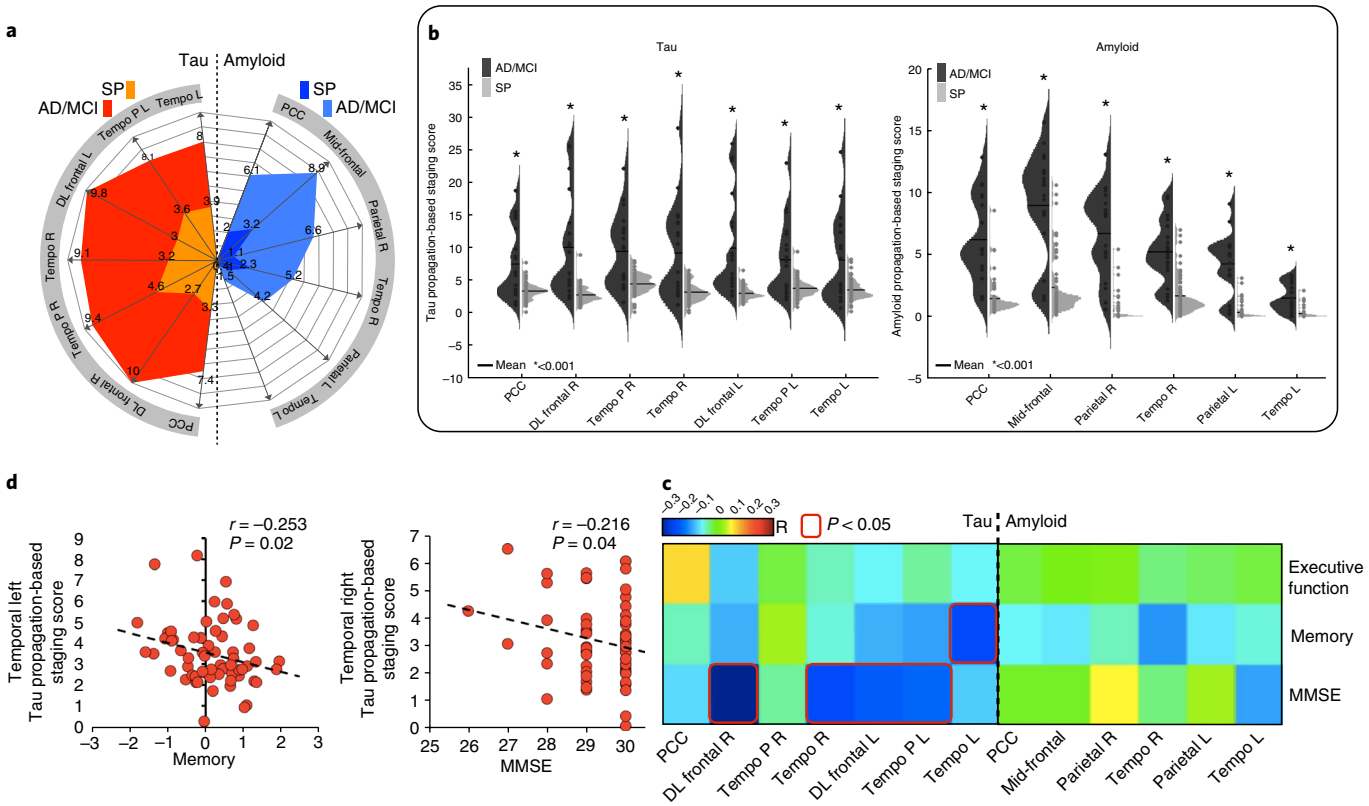

Fig. 3 | Tau and amyloid propagation-based staging. a,**b**, Characterization of propagation pathways of tau and Aβ deposits in individuals of the cross-sectional data ((SP with complete neuropsychological assessment, $n = 64$) and Alzheimer's disease (AD/MCI, $n = 19$) subjects; polar plot (**a**) and violin plots (**b**) are shown). The mean is a measure of the center in the violin plots (**b**). The smooth histograms of SP (light gray dots and histograms) and AD/MCI (dark gray dots and histograms) data in violin plots are obtained by using the cumulative histogram, a smoothening spline and the analytical derivative. In **b**, the *x* axis shows the targeted regions of interest. **c**,**d**, Characterization of the relationship between propagation pathways of tau and Aβ and cognitive levels (**c**) and tau and cognitive levels (**d**) in SP. In **d**, the *x* axis shows the cognitive scores. Two-tailed, unpaired *t*-test corrected by multiple comparisons was used in **b**, and Pearson's correlation (and the related *P* value from the one-tailed *t*-test noncorrected by multiple comparisons) was used in **c** and **d**. DL, dorsolateral; L, left; P, parietal; R, right; Tempo, temporal.

neuronal degeneration and the genetic risk factors that may underlie it. In this study, we used two unique data sets, a HABS sample with flortaucipir-PET and Pittsburgh compound B (PiB)-PET imaging data, and a sample from the AHBA with data of cortical gene expression levels of the human protein-coding transcriptome, to characterize the topological distributions and colocalizations of in vivo tau and Aβ propagation with the expression of certain genes. We found that both tau and Aβ propagation associate to a common genetic profile related to 'lipid metabolism', whereas tau propagation was related to the *MAPT* gene and an 'axon-related' genetic profile, and Aβ propagation was related to the *CLU* gene and a 'dendrite-related' genetic profile. Although we estimated detailed progression patterns using in vivo PET, it is intriguing that a previous study that matched AHBA anatomical annotations to AD regions found an association between *MAPT* expression and potential vulnerability to tau accumulation as defined by Braak and Braak staging[20]. In addition to the main findings of our study, here, we also developed a novel quantitative approach for the in vivo staging of AD pathology in humans. Thus, overall, we provide an integrative framework for investigating the neurobiological basis of imaging phenotypes in preclinical and clinical AD, as well as phenotype–genotype associations.

Although PET imaging has been able to identify and visualize Aβ protein deposits in the brain for over a decade, high-affinity radiolabels for tau protein have only recently been successfully developed[21–25]. Flortaucipir, a newly developed tracer for the imaging of tau pathology with PET, binds with high affinity to hyperphosphorylated tau pathology, for example, in regions such as the medial temporal lobe and the associative cortex, and shows potential for the detection of preclinical and clinical AD populations following the classical Braak and Braak neuropathological staging of neurofibrillary tangles[17,25,26]. Hence, it is now possible to design comprehensive side-by-side comparisons of tau and Aβ and to study the initial stages and progression of these proteinopathies. Moreover, as tau and Aβ protein depositions are not randomly distributed, but rather exhibit characteristic spatial patterns[2,27–30] that follow large-scale connectivity networks[19,31–38], the study of AD pathology networks has become essential for the understanding of the spatial distribution and potential propagation of the disease.

Previous PET neuroimaging studies have typically overlooked the temporal dimension and network nature of AD-related pathology. Conventional PET imaging analysis techniques are only sensitive to gross changes in signal intensity, ignoring the spatiotemporal or large-scale network relationships that distributed regions may exhibit in their molecular binding affinity. In this study, we provide new in vivo insights regarding network-wise longitudinal changes of tau and Aβ pathology. We developed a novel graph theory approach for detecting propagation pathways of AD pathology and found distinct propagation pathways for tau and Aβ accumulation. In particular, medial/inferior temporal lobe areas projected pathways of tau propagation toward the anterior pole, lateral and posteromedial temporal cortex and orbitofrontal cortex, whereas the PCC projected Aβ toward surrounding areas and the lateral parietal lobe. These findings support the idea that accumulation patterns of pathology evolve beyond local neighborhoods. For instance, the cross-sectional

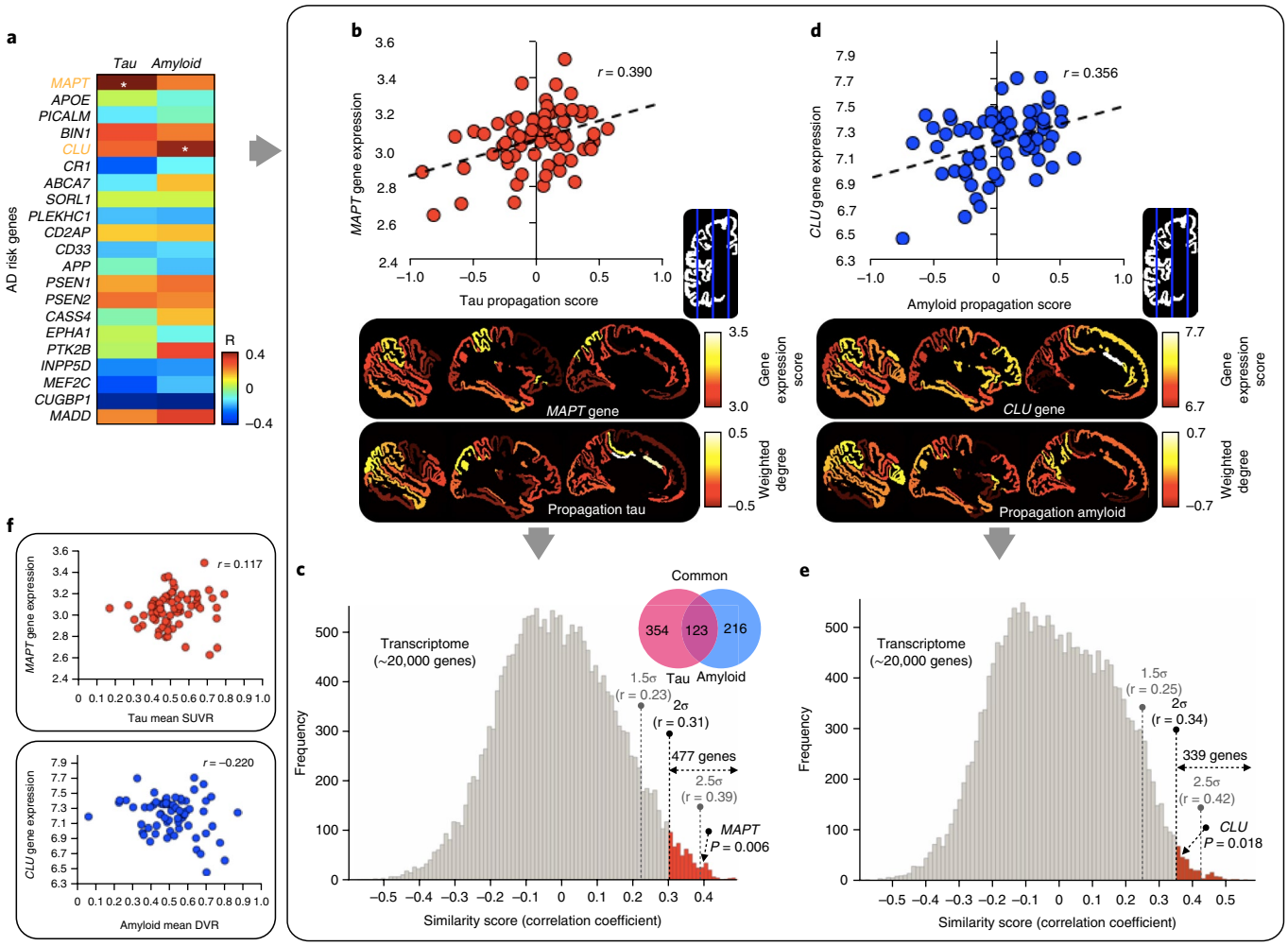

Fig. 4 | Brain colocalization of in vivo propagation patterns and Allen gene expression data. a, Matrix of similarity scores (hot scale) between in vivo propagation patterns of tau and Aβ and Allen gene expression levels of 21 previously related AD genes (the asterisks show the highest similarity scores). **b**,**d**, Scatter plots between in vivo propagation patterns of tau and *MAPT* expression (top; **b**) and Aβ and *CLU* expression (top; **d**), as well as their cortical distributions (bottom; hot color scale; **b** and **d**). **c**,**e**, Null hypothesis distributions of similarity scores between in vivo propagation patterns of tau (**c**) and Aβ (**e**) and the entire protein-coding transcriptome. Similarity scores were converted to z-scores, and the corresponding one-tailed *P* values were obtained for *MAPT* (**c**) and *CLU* (**e**) z-scores. The red areas show similarity scores above 2 s.d. **f**, Scatter plots are shown between in vivo regional intensity of tau and *MAPT* (top) and Aβ and *CLU* (bottom). Note that the scatter plot in **f** shows SUVR and DVR values that represent linearly transformed values from the original maps, including downsampling, conversion to 68-region Desikan space and whole-sample averaging of the data. Pearson's correlation was used in **a**–**f** to determine linear similarity scores between cortical maps of 68 regions (dots in **b**, **d** and **f**).

and longitudinal tau data show that temporal lobe pathology progresses distantly toward the orbitofrontal cortex and limbic areas, such as the PCC. Moreover, our results are in accordance with post-mortem histopathology characterizations[2,27,28,34,39–41], as well as recent neuroimaging descriptions[42], and open new avenues for improving current staging methods and interpreting AD-related pathology findings by accounting for observed propagation routes of pathology progression. For instance, out-degree and in-degree hubs in the cerebral cortex can be seen as regions that act as 'givers' or 'receivers' of signal over time, respectively. Here, we found that temporal cortex areas are the main 'giver' regions for tau signal in this regard. The hubness of the temporal lobe out-degree pattern explains the sequential progression of the signal from this area toward locally and distantly connected areas, such as the cingulate cortex. Thus, we speculate that the 'giving' signal property, at least for this temporal region, implies long-distance connectivity toward locations that are the 'receivers' of signal, such as the previously mentioned cingulate area (as seen in the in-degree maps). In this investigation, we developed new approaches to understand how AD-related pathology advances across specific brain systems in the living human brain. We posit that the human brain behaves as a dynamic network, even while, or even when, it undergoes neurodegeneration. The existence of hub cortical areas that drive the time-based or sequential patterns of tau and Aβ accumulation opens up new possibilities for developing more accurate staging methods that may be able to capture the network spreading nature of AD-related pathology.

Pathology studies have shown that precursor proteins, such as APP, α-secretase, β-secretase and γ-secretase, behave discordantly in patients with AD, leading to the accumulation of self-aggregating Aβ[43]. Moreover, the *APOE* ε4 allele genotype and other single-nucleotide polymorphisms in ~20 genes—although with less risk intensity—have been associated with late-onset sporadic AD in genome-wide association studies[6–9]. However, it remains unknown how genetic factors relate to the concrete progression of pathology across neuronal circuits. Thus, in this study, we focused on integrating information from in vivo propagation patterns of tau and Aβ deposits with putative genetic biomarkers expressed in the human cortex, to investigate whether the identified genetic biomarkers support

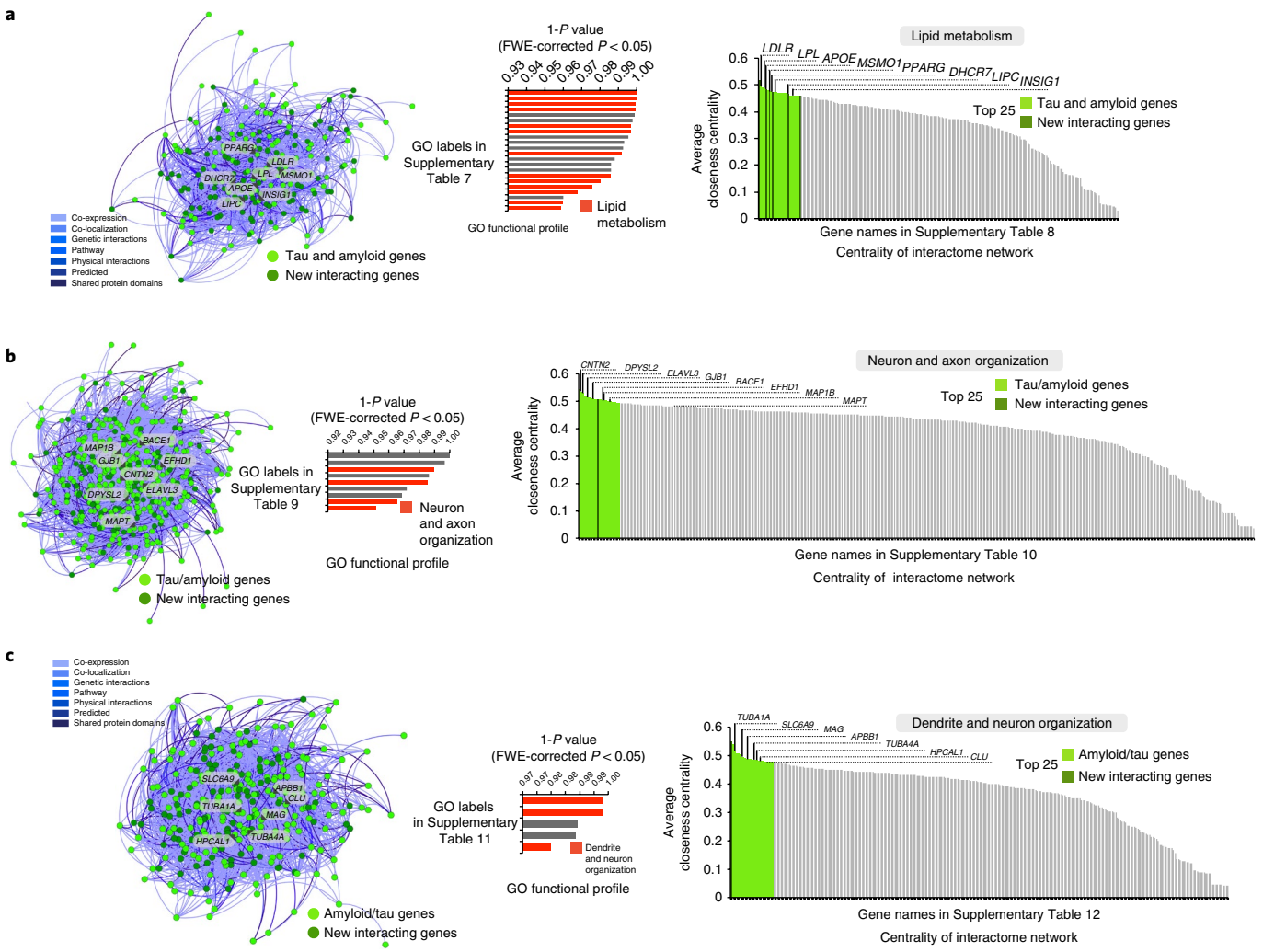

Fig. 5 | Interactome and Gene Ontology analyses of imaging genetic profiles. a–c, Interactome networks showing significant Gene Ontology (GO) overrepresented functionality (FWE-corrected $P < 0.05$) and node centrality of common (**a**), only tau (**b**) or only Aβ (**c**) genetic sets obtained from the neuroimaging genetics similarity approach (Fig. 4). The blue color scale in the interactome networks (left) shows the types of genetic interactions. The labels in the interactome networks (left) and in the centrality bar graphs (right) show genes associated to the main GO overrepresented domains (middle). The top 25 most central genes of the interactome networks are shown in green in the centrality bar graphs (right). Of note, Supplementary Tables 7, 9 and 11 show the GO functional labels and values, and Supplementary Tables 8, 10 and 12 show the list of genes and node centrality values for each interactome network.

susceptibility for network accumulation of AD pathology. We found that group-level imaging phenotypes of tau and Aβ propagation are associated with a rich set of genes that are expressed in analogous brain regions in the AHBA. These colocalizations suggest that a common background of genes devoted to lipid metabolism may possibly underlie the evolution of both tau and Aβ across specific neural systems[14]. Although the amyloid hypothesis, centered in the triggered and deleterious effects of Aβ deposits, has been the prevailing model used to explain the pathophysiology of AD, Aβ deposits do not correlate well with the clinical course, neuronal dysfunction or with cognitive performance, and anti-Aβ treatments have failed or have shown inconsistencies in altering the course of the disease[44]. Alternatively, others have emphasized the abnormal intraneuronal accumulation of hyperphosphorylated tau as a critical component in explaining the cause of AD. Specifically, postmortem studies have shown better correlation between premortem cognition and tau than Aβ[45]. However, the inter-relationships between Aβ and tau are far from being understood and some neuropathological work points toward tau inducing Aβ[46]. Here, our findings partially support the notion of an interaction between these proteinopathies. For example, *BACE1* appeared as one of the central genes in the tau-related interactome network. However, there may also be other mechanisms at higher levels of integration beyond direct spatial interactions between tau and Aβ. For instance, the set of genes common to both hallmarks of the disease is implicated in lipid metabolism, in which *APOE* seems to have a central role. Although *APOE* gene expression was not identified as directly spatially related to neither tau nor Aβ PET progression phenotypes, *APOE* displayed a critical place in the common interactome network observed in this study. Thus, it is plausible that *APOE* may influence tau and Aβ accumulation by third parties, generating a functionality that goes beyond its spatial constraints. If we consider that tau and Aβ are end-products of AD neurodegeneration, it is plausible to postulate that genetic variants along different levels of their common pathways (for example, *APOE*) may lead to the aggregation and co-occurrence of both AD pathology hallmarks, tau and Aβ. In fact, recent findings postulate that ApoE-binding sites include 1,700 gene promoter regions, implicating genes associated with trophic support, programmed cell death, microtubule disassembly, synaptic function and aging[47], processes in which tau and Aβ have

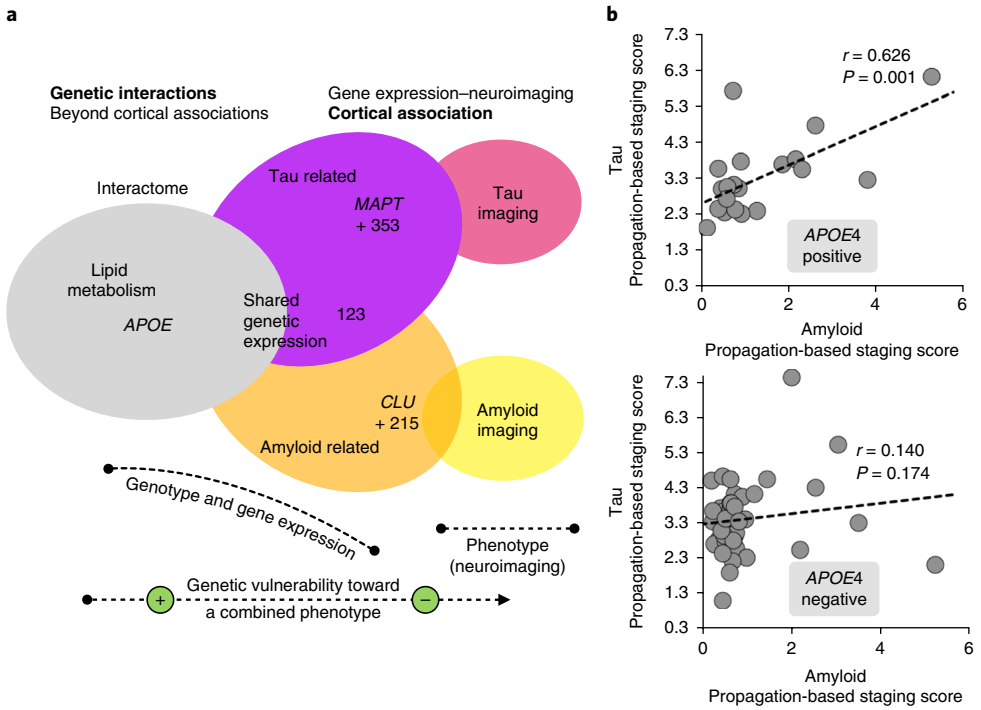

Fig. 6 | Propagation-based staging of tau and Aβ and *APOE* genotype in individuals. a, Diagram of neuroimaging–genetic relationships between in vivo PET phenotypes, cortical gene expression levels and interactome profiles aimed to identify biomarkers conferring vulnerability for tau and Aβ accumulation. **b**, Scatter plots show a linear relationship between tau and Aβ individual staging only in *APOE* ε4⁺ individuals ($n = 68$ HABS healthy adults; 21 *APOE* ε4⁺ and 47 *APOE* ε4⁻). Pearson's correlation (and the related *P* value from the one-tailed *t*-test noncorrected by multiple comparisons) was used.

been both extensively implicated. In addition, it is also likely that genetic variants of genes specifically associated with either tau or Aβ molecular pathways may confer susceptibility for a specific or predominant accumulation of one or the other. Our final findings partially support this interpretation, for example, although *APOE* ε4⁺ individuals display concomitant tau and Aβ accumulation, *APOE* ε4⁻ individuals may showcase elevated tau or Aβ accumulation but in a way in which they may be unrelated with one another, suggesting that perhaps other genes considered to be less specific to the common pathway of AD dementia could potentially also be related to the spatially different accumulation patterns of tau or Aβ, and account for the *APOE* ε4⁻ AD cases.

Over the past few decades, an intense debate has been sustained between Aβ-centrist and tau-centrist views of AD. Although our study was not designed to validate the Aβ-centrist or the tau-centrist view, it does highlight the existence of specific genetic profiles associated with either tau or Aβ PET phenotypes. More importantly, and away from these two centrist viewpoints, we observed that a common genetic background seems to embrace propagation patterns, both for tau and Aβ. In other words, our findings support that common biological sources may underlie tau and Aβ protein malfunctioning, in which *APOE* ε4⁺ could play a critical role (Fig. 6). Thus we believe that now more than ever, AD research is in need of novel approaches that integrate in vivo propagation patterns with individual genetic data to unveil idiosyncratic vulnerabilities associated with the development and trajectory of late-onset sporadic AD.

The detection and combination of in vivo patterns of tau and Aβ propagation with genetic profiles of AD risk will aid the future development of comprehensive approaches for better diagnosis and monitoring of AD, as well as for the evaluation of personalized risk to AD at earlier stages of the disease spectrum. In this study, we characterized the cortical propagation pathways of tau and Aβ pathology in a longitudinal cohort of cognitively normal adult participants and identified some of the genetic underpinnings using in situ information from a transcriptome atlas of cerebral tissue. It is important to note that our investigation only examined a fraction of all possible neuropathological events in AD-related neurodegeneration and focuses on PET data from early stages in which small sample sizes and low PET intensity values may be limitations. However, we believe that our findings offer novel avenues for enhancing the detectability of AD trajectories, for interpreting imaging and genetic information in a more integrated manner and for the future monitoring of novel therapeutic strategies.

Received: 29 January 2018; Accepted: 29 August 2018;
Published online: 29 October 2018

References

1. Braak, H. & Braak, E. Evolution of the neuropathology of Alzheimer's disease. *Acta Neurol. Scand. Suppl.* **165**, 3–12 (1996).
2. Thal, D. R., Rüb, U., Orantes, M. & Braak, H. Phases of Aβ-deposition in the human brain and its relevance for the development of AD. *Neurology* **58**, 1791–1800 (2002).
3. Braak, H., Del Tredici, K., Schultz, C. & Braak, E. Vulnerability of select neuronal types to Alzheimer's disease. *Ann. N. Y. Acad. Sci.* **924**, 53–61 (2000).
4. Wu J. W. et al. Neuronal activity enhances tau propagation and tau pathology in vivo. *Nat. Neurosci.* **19**, 1085–1092 (2016).
5. Khan, U. A. et al. Molecular drivers and cortical spread of lateral entorhinal cortex dysfunction in preclinical Alzheimer's disease. *Nat. Neurosci.* **17**, 304–311 (2014).
6. Lambert, J. C. et al. Meta-analysis of 74,046 individuals identifies 11 new susceptibility loci for Alzheimer's disease. *Nat. Genet.* **45**, 1452–1458 (2013).
7. Naj, A. C. et al. Common variants at *MS4A4/MS4A6E*, *CD2AP*, *CD33* and *EPHA1* are associated with late-onset Alzheimer's disease. *Nat. Genet.* **43**, 436–441 (2011).
8. Roussotte, F. F. et al. Combined effects of Alzheimer risk variants in the *CLU* and *ApoE* genes on ventricular expansion patterns in the elderly. *J. Neurosci.* **34**, 6537–6545 (2014).
9. Karch, C. M. & Goate, A. M. Alzheimer's disease risk genes and mechanisms of disease pathogenesis. *Biol. Psychiatry* **77**, 43–51 (2015).

10. Beecham, G. W. et al. Genome-wide association meta-analysis of neuropathologic features of Alzheimer's disease and related dementias. *PLoS Genet.* **10**, e1004606 (2014).
11. Allen, M. et al. Association of *MAPT* haplotypes with Alzheimer's disease risk and *MAPT* brain gene expression levels. *Alzheimers Res. Ther.* **6**, 39 (2014).
12. Shen, E. H., Overly, C. C. & Jones, A. R. The Allen Human Brain Atlas. Comprehensive gene expression mapping of the human brain. *Trends Neurosci.* **35**, 711–714 (2012).
13. Jones, A. R., Overly, C. C. & Sunkin, S. M. The Allen Brain Atlas: 5 years and beyond. *Nat. Rev. Neurosci.* **10**, 821–828 (2009).
14. Shi, Y. et al. ApoE4 markedly exacerbates tau-mediated neurodegeneration in a mouse model of tauopathy. *Nature* **549**, 523–527 (2017).
15. Sperling, R. A. et al. Toward defining the preclinical stages of Alzheimer's disease: recommendations from the National Institute on Aging-Alzheimer's Association workgroups on diagnostic guidelines for Alzheimer's disease. *Alzheimers Dement.* **7**, 280–292 (2011).
16. Dagley, A. et al. Harvard Aging Brain Study: dataset and accessibility. *Neuroimage* **144**, 255–258 (2017).
17. Johnson, K. A. et al. Tau positron emission tomographic imaging in aging and early Alzheimer disease. *Ann. Neurol.* **79**, 110–119 (2016).
18. Sepulcre, J., Sabuncu, M., Becker, A., Sperling, R. & Johnson, K. In vivo characterization of the early states of the amyloid-beta network. *Brain* **136**, 2239–2252 (2013).
19. Sepulcre, J. et al. In vivo tau, amyloid, and gray matter profiles in the aging brain. *J. Neurosci.* **36**, 7364–7374 (2016).
20. Freer, R. et al. A protein homeostasis signature in healthy brains recapitulates tissue vulnerability to Alzheimer's disease. *Sci. Adv.* **2**, e1600947 (2016).
21. Chien, D. et al. Early clinical PET imaging results with the novel PHF-tau radioligand [F18]-T807. *J. Alzheimers Dis.* **34**, 457–468 (2013).
22. Maruyama, M. et al. Imaging of tau pathology in a tauopathy mouse model and in Alzheimer patients compared to normal controls. *Neuron* **79**, 1094–1108 (2013).
23. Okamura, N. et al. Novel ^{18}F-labeled arylquinoline derivatives for noninvasive imaging of tau pathology in Alzheimer disease. *J. Nucl. Med.* **54**, 1420–1427 (2013).
24. Villemagne, V. L. et al. In vivo evaluation of a novel tau imaging tracer for Alzheimer's disease. *Eur. J. Nucl. Med. Mol. Imaging* **41**, 816–826 (2014).
25. Schöll, M. et al. PET imaging of tau deposition in the aging human brain. *Neuron* **89**, 971–982 (2016).
26. Sepulcre, J. et al. Hierarchical organization of tau and amyloid deposits in the cerebral cortex. *JAMA Neurol.* **74**, 813–820 (2017).
27. Arnold, S. E., Hyman, B. T., Flory, J., Damasio, A. R. & Van Hoesen, G. W. The topographical and neuroanatomical distribution of neurofibrillary tangles and neuritic plaques in the cerebral cortex of patients with Alzheimer's disease. *Cereb. Cortex* **1**, 103–116 (1991).
28. Braak, H. & Braak, E. Neuropathological stageing of Alzheimer-related changes. *Acta Neuropathol.* **82**, 239–259 (1991).
29. Hyman, B. T., Van Hoesen, G. W., Damasio, A. R. & Barnes, C. L. Alzheimer's disease: cell-specific pathology isolates the hippocampal formation. *Science* **225**, 1168–1170 (1984).
30. Kalus, P., Braak, H., Braak, E. & Bohl, J. The presubicular region in Alzheimer's disease: topography of amyloid deposits and neurofibrillary changes. *Brain Res.* **494**, 198–203 (1989).
31. Buckner, R. L. et al. Cortical hubs revealed by intrinsic functional connectivity: mapping, assessment of stability, and relation to Alzheimer's disease. *J. Neurosci.* **29**, 1860–1873 (2009).
32. Greicius, M. Resting-state functional connectivity in neuropsychiatric disorders. *Curr. Opin. Neurol.* **21**, 424–430 (2008).
33. Greicius, M. D., Srivastava, G., Reiss, A. L. & Menon, V. Default-mode network activity distinguishes Alzheimer's disease from healthy aging: evidence from functional MRI. *Proc. Natl Acad. Sci. USA* **101**, 4637–4642 (2004).
34. Kuchibhotla, K. V. et al. Neurofibrillary tangle-bearing neurons are functionally integrated in cortical circuits in vivo. *Proc. Natl Acad. Sci. USA* **111**, 510–514 (2014).
35. Seeley, W. W., Crawford, R. K., Zhou, J., Miller, B. L. & Greicius, M. D. Neurodegenerative diseases target large-scale human brain networks. *Neuron* **62**, 42–52 (2009).
36. Zhou, J., Gennatas, E. D., Kramer, J. H., Miller, B. L. & Seeley, W. W. Predicting regional neurodegeneration from the healthy brain functional connectome. *Neuron* **73**, 1216–1227 (2012).
37. Sepulcre, J. et al. Tau and amyloid β proteins distinctively associate to functional network changes in the aging brain. *Alzheimers Dement.* **13**, 1261–1269 (2017).
38. Hansson, O. et al. Tau pathology distribution in Alzheimer's disease corresponds differentially to cognition-relevant functional brain networks. *Front. Neurosci.* **11**, 167 (2017).
39. Serrano-Pozo, A., Frosch, M. P., Masliah, E. & Hyman, B. T. Neuropathological alterations in Alzheimer disease. *Cold Spring Harb. Perspect. Med.* **1**, a006189 (2011).
40. Bero, A. W. et al. Neuronal activity regulates the regional vulnerability to amyloid-β deposition. *Nat. Neurosci.* **14**, 750–756 (2011).
41. Marquié, M. et al. Validating novel tau positron emission tomography tracer [F-18]-AV-1451 (T807) on postmortem brain tissue. *Ann. Neurol.* **78**, 787–800 (2015).
42. Jacobs, H. I. L. et al. Structural tract alterations predict downstream tau accumulation in amyloid-positive older individuals. *Nat. Neurosci.* **21**, 424–431 (2018).
43. Marioni, R. E. et al. Genetic stratification to identify risk groups for Alzheimer's disease. *J. Alzheimers Dis.* **57**, 275–283 (2017).
44. De Strooper, B. & Karran, E. The cellular phase of Alzheimer's disease. *Cell* **164**, 603–615 (2016).
45. Nelson, P. T. et al. Correlation of Alzheimer disease neuropathologic changes with cognitive status: a review of the literature. *J. Neuropathol. Exp. Neurol.* **71**, 362–381 (2013).
46. Duyckaerts, C. et al. PART is part of Alzheimer disease. *Acta Neuropathol.* **129**, 749–756 (2015).
47. Theendakara, V. et al. Direct transcriptional effects of apolipoprotein E. *J. Neurosci.* **36**, 685–700 (2016).

Acknowledgements

We thank the investigators and staff of the Harvard Aging Brain Study, Massachusetts Alzheimer's Disease Research Center, the individual research participants, and their families and caregivers. We also thank the PET Core of the MGH, the Harvard Center for Brain Science Neuroimaging Core and the Athinoula A. Martinos Center for biomedical imaging support. This research was supported by grants from the National Institutes of Health (NIH) (K23-EB019023 to J.S.; T32EB013180 to L.O.-T.; R01HL137230 and P41-EB022544 to G.E.-F.; R01-AG027435-S1 to R.A.S. and K.A.J.; P50-AG00513421 and R01AG046396 to K.A.J. and R.A.S.; P01-AG036694 to R.A.S. and K.A.J.; and RF1AG052653 to Q.L.); Massachusetts ADRC; Alzheimer's Association (NIRG-11-205690 to J.S.; IIRG-06-32444 to R.A.S. and K.A.J.; and ZEN-10-174210 to K.A.J.); and the Alzheimer Forschung Initiative e.V. (to M.J.G.). The authors declared no potential conflicts of interest with respect to the research, authorship and/or publication of this article.

Author contributions

J.S. contributed to the design, analysis and interpretation of the data and preparation of the manuscript. M.J.G. contributed to the design, analysis and interpretation of the data and preparation of the manuscript. F.d.U. contributed to the analysis of the data and preparation of the manuscript. L.O.-T. contributed to the analysis of the data and preparation of the manuscript. I.D. contributed to the analysis and interpretation of the data and preparation of the manuscript. H.-S.Y. contributed to the analysis of the data and preparation of the manuscript. H.I.L.J. contributed to the interpretation of the data and preparation of the manuscript. B.H. contributed to the interpretation of the data and preparation of the manuscript. Q.L. contributed to the interpretation of the data and preparation of the manuscript. G.E.-F. contributed to the interpretation of the data and preparation of the manuscript. R.A.S. contributed to the design and interpretation of the data and preparation of the manuscript. K.A.J. contributed to the design and interpretation of the data and preparation of the manuscript.

Competing interests

The authors declare no competing interests.

Additional information

Supplementary information is available for this paper at https://doi.org/10.1038/s41591-018-0206-4.

Reprints and permissions information is available at www.nature.com/reprints.

Correspondence and requests for materials should be addressed to J.S.

Publisher's note: Springer Nature remains neutral with regard to jurisdictional claims in published maps and institutional affiliations.

Methods

Participants. We included 88 clinically normal participants from the HABS ((mean age (s.d.): 72.24 years (11.63), male/female: 43/45); see Supplementary Table 1 for detailed demographics and clinical characteristics), out of which 19 also had a 2-year follow-up assessment ((mean age (s.d.): 75.63 years (5.95), male/female: 11/8). Apart from the main longitudinal sample, we included an additional longitudinal sample of 24 HABS individuals ((mean age (s.d.): 76.09 years (5.66), male/female: 9/15); see Supplementary Table 2 for detailed demographics and clinical characteristics) for validation and replication of our propagation method and findings. This replication sample was also used to investigate PVC effects on PET images. We also included 19 participants previously classified as cognitively impaired by memory clinics of Harvard School of Medicine–affiliated hospitals, including diagnoses of MCI or AD dementia (mean age (s.d.): 67.45 years (9.12), male/female: 14/5; mean Clinical Dementia Rating–Sum of Boxes (s.d.): 3.82 (2.91); mean Mini-Mental State Examination (MMSE): 24.47 (4.95)). As part of HABS, participants undergo multiple neuroimaging sessions, *APOE* genotyping and an annual neuropsychological testing that includes the Preclinical Alzheimer's Cognitive Composite. The Preclinical Alzheimer's Cognitive Composite combines logical memory delayed recall, MMSE total score, Wechsler Adult Intelligence Scale–revised digit symbol coding and the free and cued selective reminding test[48]. Direct genotyping of *APOE* rs7412 and rs429358 was performed at the Harvard Neurodiscovery Center to derive *APOE* haplotypes. Participants are originally included if they have a score of 0 on the Clinical Dementia Rating scale, a MMSE score of ≥25 and if they perform within education-adjusted norms on the logical memory delayed recall test (>10 for ≥16 years of education, >6 for 8–15 years of education and >4 for <8 years of education). All participants undergo at least one comprehensive medical and neurological evaluation and must not have any medical or neurological disorders at enrollment that could contribute to their cognitive abilities. The presence of clinical depression (Geriatric Depression Scale above 11/30) or other psychiatric illnesses, history of alcoholism, drug abuse, head trauma or a family history of autosomal dominant AD dementia were exclusionary criteria. All participants took part in the study using protocols and informed consent procedures approved by the Partners Human Research Committee at the Massachusetts General Hospital. Further information on study design is available in the Nature Research Reporting Summary.

MRI and PET acquisition and preprocessing procedures. All participants underwent a magnetic resonance imaging (MRI) image acquisition of the whole head on a Siemens 3 Tesla Tim Trio system using a 12-channel phased-array head coil that included a T1-weighted MPRAGE (magnetization-prepared rapid gradient-echo) scan using the following parameters: repetition time (TR) = 6,400 ms, echo time (TE) = 2.8 ms, flip angle = 8°, inversion time (TI) = 900 ms and a voxel size of 1.0 × 1.0 × 1.2 mm. We used SPM12 (Wellcome Centre for Human Neuroimaging, University College London, London, UK; http://www.fil.ion.ucl.ac.uk/spm), running under MATLAB v8.0 (Mathworks Inc.), for image preprocessing and normalization of anatomical T1-weighted MRI volumes. We used the VBM8 toolbox for voxel-based morphometry analysis of the anatomical T1-weighted magnetic resonance images[49]. Briefly, after spatial normalization of all images from native to normalized Montreal Neurological Institute/International Consortium for Brain Mapping (MNI/ICBM) space, images were segmented into gray matter, white matter and cerebrospinal fluid. Then, we selected gray matter–modulated and 10-mm full-width at half-maximum Gaussian kernel smoothed images for further analysis to control for gray matter volume intensity. All participants had two PET imaging acquisitions at the Massachusetts General Hospital PET facility: (i) flortaucipir (also known as ^{18}F-T807 or ^{18}F-AV-1451) PET that binds to tau in neurofibrillary tangles and neurites[21], and (ii) a ^{11}C-labeled PiB, *N*-methyl ^{11}C-2-(4-methylaminophenyl)-6-hydroxybenzothiazole (^{11}C-PiB) PET that binds to fibrillary Aβ plaques[50]. Flortaucipir PET parameters were as follows: 10 mCi of ^{18}F-T807, 3D-mode static protocol of 20-min acquisition from 80–100 min; 63 image planes, 15.2-cm axial field of view, 5.6-mm transaxial resolution and 2.4-mm slice interval; 4 × 300-s frames at 80 min postinjection followed by a 6-min transmission[17]. The final intensity ^{18}F-T807 maps were obtained, calculating the SUVR using a cerebellar gray reference region. Conversely, ^{11}C-PiB PET parameters were as follows: following a transmission scan, 10–15 mCi ^{11}C-PiB was injected intravenously as a bolus and followed immediately by a 60-min dynamic PET scan in 3D mode (63 image planes, 15.2-cm axial field of view, 5.6-mm transaxial resolution and 2.4-mm slice interval; 69 frames: 12 × 15 s, 57 × 60 s)[17,50]. PiB retention intensity was expressed as the DVR at each voxel and was calculated using Logan's graphical method, using a cerebellar gray reference region. Corrections for normalization, dead time, random coincidences, scattered radiation and attenuation were performed and each frame was evaluated to verify adequate count statistics and the absence of head motion. Using SPM12, all PET data in native space were co-registered with their corresponding anatomical T1-weighted MRI images and spatially normalized into MNI standard space using the normalization parameters obtained from the T1-weighted MRI normalization. Our processing pipeline also included an outlier detection approach based on the assessment of normally distributed values of each voxel within our sample to ensure that only voxels with a normal continuum range of PET values were entered in the regression analysis[51] (Supplementary Fig. 2). All PET data were downsampled from the normalized space to 8-mm isotropic voxel to study the high-dimensional data without computational limitations.

Directional graph theory regression and statistics. In contrast to conventional analysis approaches in PET imaging in which only regional intensity is investigated, here, we studied PET signal changes using a novel DGTR approach to investigate network-based changes between regions of the human brain (Supplementary Fig. 1a,b; association matrices and network diagrams). Furthermore, conventional analysis approaches in PET imaging fail to infer network changes and network temporal directionality, as they are not designed to utilize the spatiotemporal PET patterns across different brain systems. Thus, DGTR may provide novel information about network-level stages of accumulation of pathology, as well as information about potential pathways of pathology spread associated with progression of the disease through brain tissue.

In DGTR, we assume that PET imaging data are in proximity to a submanifold and are Gaussian smooth signals on a weighted graph in a discretized approximation, as verified in many relevant works[52–54]. To that end, we first computed PET-based association matrices (or PET-based connectivity matrices) between all pairs of voxels across the gray matter of the brain, and built group-level network graphs for the cross-sectional samples (Supplementary Fig. 1a and within time 1 connectivity in Fig. 1c) and longitudinal study samples (Supplementary Fig. 1b and between time 1 and time 2 connectivity in Fig. 1c). We used a partial correlation approach to calculate intersubject associations of DVR or SUVR values between all pairs of voxels of the brain controlled for MRI atrophy by regressing out the influence of gray matter volume intensities. We then designated seeds based on specific a priori regions. We selected the inferior temporal cortex and PCC owing to their early high-intensity values in PET in vivo studies. These two regions of interest were obtained from our previous studies based on PET neuroimaging independent data sets[17,26]. We used the PCC and inferior temporal seed-based analysis to compare our PET data with and without PVC adjustment using the extended Müller–Gartner method as previously implemented for FreeSufer[42,55,56]. As other seeds may also be relevant in this context, particularly if early histological data are taken into account[45,46,49], we included additional seeds in the analysis, such as the entorhinal cortex and the medial prefrontal cortex (Supplementary Fig. 3). The entorhinal cortex and medial prefrontal cortex (the medial orbitofrontal cortex and the rostral anterior cingulate cortex) regions of interest were based on the Desikan–Killiany atlas[57]. In the particular case of tau data, we controlled our partial regression analysis not just by regressing out the voxel-level gray matter volume information but also by excluding the signal intensity of the plexus choroideus, which may strongly correlate with the signal intensity of medial temporal lobe structures owing to spatial proximity[17]. Signal from the choroid plexus was removed using the region of interest from the Desikan–Killiany subcortical atlas[57]. In the cross-sectional propagation model, the partial correlation coefficient between each brain voxel and the a priori seed region was interpreted as a predictor of pathology propagation[18]. In the longitudinal propagation model, the partial correlation coefficient between each brain voxel and the a priori seed region was interpreted as an observation of pathology propagation. For the particular analysis of the longitudinal study sample, we computed connectivity matrices between time 1 and time 2 (red connectivity in the network diagram; Supplementary Fig. 1b,c). Following the Supplementary Fig. 1c example, if we were assessing connectivity profiles between voxel *b* and voxel *d*, we would compute the partial correlations of the PET values across the sample between voxel *b* in time 1 and voxel *d* in time 2, as well as between voxel *b* in time 2 and voxel *d* in time 1. The partial correlation (PC) can be solved with the *t*-statistic, studying the effect of the two variables and removing the effect of atrophy by using multiple regression as shown in the equation (1):

$$\mathrm{PC}(b,d) = \frac{t_{b,d}}{\sqrt{t_{b,d}^2 + \mathrm{resdf}}} \quad (1)$$

where PC(*b*,*d*) represents the partial correlation of node *b* in time 1 with node *d* in time 2, removing the effects of atrophy; $t_{b,d}$ is the *t*-statistic looking at the effect of node *d* in time 2 on our dependent node *b* in time 1 (in the multiple regression model, the dependent variable *y* are the values of node *b* in time 1, and the design matrix *X* is defined by the intercept, values of node *d* in time 2 and atrophy values in *b* and *d*); and resdf is the residual degrees of freedom.

Once all possible interactions between pairs of voxels in the brain have been calculated, we performed statistical comparisons between connectivity profiles of voxels. Again, given the previous example, we can compare the connectivity profiles of voxel *b* to determine whether differences exist between the distributions of its partial correlation values across the two temporal conditions: (i) voxel *b* in time 1 against the rest of the voxels in time 2; and (ii) voxel *b* in time 2 against the rest of the voxels in time 1. Next, we used the two-tailed paired *t*-statistic to assess the significance (*P*) of this comparison per node (equations (2) and (3)):

$$s^2 = \frac{\sum_{i=1}^{n} (\mathrm{PC}(b,i) - \mathrm{PC}(i,b))^2 - \frac{\left(\sum_{i=1}^{n} (\mathrm{PC}(b,i) - \mathrm{PC}(i,b))\right)^2}{n}}{n-1} \quad (2)$$

$$P\ \text{value}(b) = 2\left(1-\text{cdf}\left(\left|\frac{\frac{\sum_{i=1}^{n}(\text{PC}(b,i)-\text{PC}(i,b))}{n}}{\sqrt{\frac{s^2}{n}}}\right|\right)\right) \quad (3)$$

where s^2 represents the variance of the data; n is the number of voxels; i represents the voxels of the brain from 1 to n; and cdf is the cumulative distribution function to compute the t-statistic.

Next, all within-voxel statistical comparisons between paired conditions were corrected for multiple comparisons to eliminate connectivity profiles that represent false positives by using a false discovery rate correction[58] at a q level of 0.05. Later, all connectivity profiles of false discovery rate-surviving voxels were entered in the next calculation (dark nodes in Supplementary Fig. 1c), in which we computed the final connectivity scores by subtracting the partial correlation values between conditions (equation (4)):

$$D(b,d) = \text{PC}(b,d) - \text{PC}(d,b) \quad (4)$$

This approach provided the directional (time-based) connectivity relationships between voxels. For instance, if voxel b signal at time 1 explained voxel d signal at time 2 with a statistically significant greater magnitude than how voxel d signal at time 1 explained voxel b signal at time 2, then a directional connection from voxel b to voxel d was established (out-connectivity from b to d; Supplementary Fig. 1c). The resulting matrices D of this analysis served as inputs for the subsequent weighted-degree computations. We evaluated the overall degree of each voxel to explain hub-based directional relationships in the longitudinal data—independent from a priori selection of specific seed regions—by calculating the out-weighted degree (WD_{out}) and the in-weighted degree (WD_{in}) according to equations (5) and (6), where i and j represent the voxels of the brain:

$$WD_{\text{out}}(i) = \sum_{j=1}^{n} \max(D(i,j), 0) \quad (5)$$

$$WD_{\text{in}}(i) = \sum_{j=1}^{n} \max(-D(i,j), 0) \quad (6)$$

Of note, seed-based analysis was performed by extracting the connections (cross-sectional) or out-connections (longitudinal) from a priori regions of interest. We investigated the spatial similarity between the cross-sectional predicted and the longitudinal observed maps using a voxel-level linear correlation approach.

Cortical space visualizations of the seed-based and weighted-degree results were generated using Caret software (PALS surface (PALS-B12)[59]; interpolated algorithm and multifiducial mapping). To increase spatial comparability across PET modalities, the result maps were z-score normalized before visualization.

Subject-level analysis using a propagation-based method. Based on the out-degree and in-degree propagation patterns determined by the DGTR approach, we developed a framework to characterize individualized pathological levels for tau and Aβ in participants. We further hypothesized that subject-level tau and Aβ levels determined by our approach would relate to specific rates of cognitive decline and other clinical features across the clinical spectrum of AD. Despite extensive research, it remains difficult to provide prognoses toward AD progression. There are several reasons for this. Current in vivo staging approaches for tau and amyloid are based on qualitative approximations of a priori regions derived from post-mortem histological studies that suffer from sampling limitations, low spatial resolution level and a lack of temporal information. Moreover, standard classification approaches for Aβ PET imaging rely on broad cortical composite regions of interest, such as the frontal, lateral parietal, lateral temporal and retrosplenial cortices—also known as FLR regions—that help to dichotomize individuals into simple Aβ-positive or Aβ-negative categories. However, this approach simplifies the underlying nature of AD pathology and makes it difficult to investigate the complex relationships between imaging features and clinical or cognitive scores. Recent work has shown that consistent regional staging models for both tau and Aβ can be extrapolated directly from cross-sectional PET imaging data[60,61]. Here, we expand on these in vivo staging approaches by developing a high spatiotemporal resolution and longitudinal propagation-based method to quantitatively characterize, understand and monitor AD pathology in early phases. This is especially relevant for tau PET imaging, which has been associated with spreading tracer retention in samples ranging from cognitively normal to MCI and to AD individuals, and has been strongly related with cognitive decline[26,41,62].

Although we cannot build directional graphs from a subject-level tau or Aβ PET image, we can assume that data from individuals are embedded at the group-level directional graph. Thus, we extracted tau and Aβ PET SUVR and DVR intensities at the individual level using masks from our previous section of out-degree and in-degree propagation pathways (templates created from group-level neuroimaging patterns above two standard deviations (2σ)). We built a propagation-based staging score per each propagation pathway from the in-degree template by extracting their tau or Aβ intensity and multiplying it by the sum of all intensities from the out-degree template. We evaluated the clinical relevance of our method and assessed individual patterns of propagation pathways derived from DGTR by analyzing its relationship with clinical diagnosis (that is, SP versus AD/MCI), as well as with individual neuropsychological profiles of SP individuals, including memory and executive function scores. We used a memory z-scores composite that includes the delayed recall scores of the selective reminding test, the free recall of the free and cued selective reminding test and the delayed recall of the logical memory test[63]. The statistical assessment was carried out using linear regression and two-tailed, unpaired t-test corrected by multiple comparisons.

Brain colocalization analysis between propagation patterns and genetic transcriptome. In this section, we used a prioristic knowledge of AD risk genes, as well as data-driven approaches based on the full genome-wide (protein-coding) transcriptome of the AHBA to delineate the cortical genetic profiles associated with the spread of AD pathology and to investigate the neurobiological role of the genetic–imaging associations. In particular, we used a surface anatomical transformation of the cortical transcription profiles of 20,737 protein-coding genes, based on 58,692 measurements of gene expression in 3,702 brain samples obtained from 6 adult human participants of the AHBA[64] (see Supplementary Table 3 for demographic and brain sample details). This anatomical transformation used mapping of the 6 individual matrices of regional gene expression (gene × MNI coordinate) to 68 prespecified cortical brain regions defined in the Desikan–Killiany atlas[57] covering the entire cortex, which enabled intersubject averaging (median values) of the regional gene expression levels. We also converted the hubs maps (sum of out-degree and in-degree hubs maps) obtained from the DGTR section into the Desikan–Killiany atlas space and vectorized both imaging and AHBA transcriptome genetic data. Then, we computed the cortical spatial similarity among imaging and genetic maps using Pearson's correlation of the magnitude of cortical profiles across the Desikan–Killiany areas (Supplementary Fig. 1d). As a first step, we identified from the literature previously described genes that are associated with tau and Aβ processing or that confer risk to clinical AD[6–11]. These selected candidate genes were: *MAPT*, *APOE*, *PICALM*, *BIN1*, *CLU*, *CR1*, *ABCA7*, *SORL1*, *PLEKHCI*, *CD2AP*, *CD33*, *APP*, *PSEN1*, *PSEN2*, *CASS4*, *EPHA1*, *PTK2B*, *INPPSD*, *MEF2C*, *CUGBPI* and *MADD*. We obtained the spatial cortical similarity (or co-localizations) between our AD-related imaging maps (in vivo tau and Aβ longitudinal propagation maps) and expression maps of each of these 21 AD-related genes. Then, we assessed the statistical meaning of these co-localizations by building null hypothesis distributions with the colocalizations between the observed propagation maps and the entire protein-coding transcriptome (cortical gene expression levels of 20,737 genes). The exact P values for specific colocalizations between imaging patterns and genes were obtained from the corresponding z-scores based on the null distribution. We delineated the cortical genetic profiles associated with the propagation of AD pathology in a data-driven approach, by determining for each PET modality all of the genes of the protein-coding transcriptome that met the statistical significance threshold. We considered 2 standard deviations above the transcriptome mean as the statistically significant level.

Interactome and Gene Ontology analysis. Our first analysis focused on investigating spatial similarity between PET pathology propagation patterns and cortical gene expression of select AD risk genes, providing information about brain pathology–gene expression colocalizations. Next, we investigated whether the data-driven genetic imaging profiles, obtained from the similarity analysis between propagation patterns and the full protein-coding transcriptome, display specific biological functionality. Using interactome and over-representation analysis, we studied genetic interactions among the identified set of genes beyond their spatial co-localizations in the cortex. We identified the role of each gene in the interactome analysis using node-level closeness centrality and relied on knowledge-guided insight to guide our understanding of the biological processes and cellular component functions of genetic profiles, using annotations from Gene Ontology[65]. We used Genemania (http://www.genemania.org)[66] and Cytoscape (www.cytoscape.org)[67] software for the interactome analysis and centrality assessment of our gene query lists, in which the weight of genetic associations was based on a composite gene–gene interaction profile from coexpressions, colocalizations, genetic interactions, pathways, predicted physical interactions and shared protein domains[66]. To avoid any arbitrary threshold when selecting neighborhoods associated to gene sets, we obtained 10 interactome networks per query list using a range of neighborhoods from 10 to 100. We obtained a single interactome network per list by calculating the mean weights of the 10 interactome networks. Finally, we used a binomial test (FWE correction at $P < 0.05$ level) and select parent terms of >3-fold in the Gene Ontology over-representation analysis to describe genetic annotation-based functionality[65].

Reporting Summary. Further information on research design is available in the Nature Research Reporting Summary linked to this article.

Code availability. All codes related to PET imaging analysis are available for the research community from the corresponding author (J.S.) upon request for the purpose of scientific investigation, teaching or the planning of clinical research studies.

Data availability

All neuroimaging and clinical data that support the findings of this study are available from https://nmr.mgh.harvard.edu/lab/harvard-aging-brain-study/public-data-releases. HABS data curation is overseen by Aaron P. Schultz (aschultz@nmr.mgh.harvard.edu) at the Martinos Center for Biomedical Imaging, Massachusetts General Hospital, Harvard Medical School, Boston, MA.

References

48. Mormino, E. C. et al. Early and late change on the preclinical Alzheimer's cognitive composite in clinically normal older individuals with elevated amyloid β. *Alzheimers Dement.* **13**, 1004–1012 (2017).
49. Ashburner, J. & Friston, K. J. Voxel-based morphometry—the methods. *Neuroimage* **11**, 805–821 (2000).
50. Mathis, C. A. et al. Synthesis and evaluation of ^{11}C-labeled 6-substituted 2-arylbenzothiazoles as amyloid imaging agents. *J. Med. Chem.* **46**, 2740–2754 (2003).
51. Grubbs, F. E. Procedures for detecting outlying observations in samples. *Technometrics* **11**, 1–21 (1969).
52. Donoho, D. L. & Grimes, C. Image manifolds which are isometric to Euclidean space. *J. Math. Imaging Vis.* **23**, 5–24 (2005).
53. Meyer, F. G. & Shen, X. Perturbation of the eigenvectors of the graph Laplacian: application to image denoising. *Appl. Comput. Harmon. Anal.* **36**, 326–334 (2014).
54. Zhang, F. & Hancock, E. R. Graph spectral image smoothing using the heat kernel. *Pattern Recognit.* **41**, 3328–3342 (2008).
55. Greve, D. N. et al. Cortical surface-based analysis reduces bias and variance in kinetic modeling of brain PET data. *Neuroimage* **92**, 225–236 (2014).
56. Hanseeuw, B. J. et al. Fluorodeoxyglucose metabolism associated with tau–amyloid interaction predicts memory decline. *Ann. Neurol.* **81**, 583–596 (2017).
57. Desikan, R. S. et al. An automated labeling system for subdividing the human cerebral cortex on MRI scans into gyral based regions of interest. *Neuroimage* **31**, 968–980 (2006).
58. Benjamini, Y. & Hochberg, Y. Controlling the false discovery rate: a practical and powerful approach to multiple testing. *J. R. Stat. Soc.* **57**, 289–300 (1995).
59. Van Essen, D. C. A Population-Average, Landmark- and Surface-based (PALS) atlas of human cerebral cortex. *Neuroimage* **28**, 635–662 (2005).
60. Cho, H. et al. In vivo cortical spreading pattern of tau and amyloid in the Alzheimer disease spectrum. *Ann. Neurol.* **80**, 247–258 (2016).
61. Grothe, M. J. et al. In vivo staging of regional amyloid deposition. *Neurology* **89**, 2031–2038 (2017).
62. Chhatwal, J. P. et al. Temporal T807 binding correlates with CSF tau and phospho-tau in normal elderly. *Neurology* **87**, 920–926 (2016).
63. Hedden, T. et al. Cognitive profile of amyloid burden and white matter hyperintensities in cognitively normal older adults. *J. Neurosci.* **32**, 16233–16242 (2012).
64. French, L. & Paus, T. A FreeSurfer view of the cortical transcriptome generated from the Allen Human Brain Atlas. *Front. Neurosci.* **9**, 1–5 (2015).
65. Ashburner, M. et al. Gene Ontology: tool for the unification of biology. *Nat. Genet.* **25**, 25–29 (2000).
66. Mostafavi, S., Ray, D., Warde-Farley, D., Grouios, C. & Morris, Q. GeneMANIA: a real-time multiple association network integration algorithm for predicting gene function. *Genome Biol.* **9**, S4 (2008).
67. Lopes, C. T. et al. Cytoscape Web: an interactive web-based network browser. *Bioinformatics* **27**, 2347–2348 (2011).

nature research

Corresponding author(s): Jorge Sepulcre

Life Sciences Reporting Summary

Nature Research wishes to improve the reproducibility of the work that we publish. This form is intended for publication with all accepted life science papers and provides structure for consistency and transparency in reporting. Every life science submission will use this form; some list items might not apply to an individual manuscript, but all fields must be completed for clarity.

For further information on the points included in this form, see Reporting Life Sciences Research. For further information on Nature Research policies, including our data availability policy, see Authors & Referees and the Editorial Policy Checklist.

Please do not complete any field with "not applicable" or n/a. Refer to the help text for what text to use if an item is not relevant to your study.
For final submission: please carefully check your responses for accuracy; you will not be able to make changes later.

Experimental design

1. Sample size

Describe how sample size was determined.

Our study included three data-sets of tau and amyloid PET images: one cross-sectional (N=69) and two longitudinal (N=19 & N=24) study samples of adult individuals (non-overlapping samples). As our analyses were based on graph regression models, we calculated the sample size of the cross-sectional group based on the power to detect an effect of Cohen's d=0.40 with a power of 0.95 (1-β error probability) and α error probability of 0.05 (software G*Power V3.1.2). This power analysis indicated a minimal sample size of N=63. Therefore our cross-sectional sample employed to predict pathology propagation using voxel-based graphs of PET images were sufficient to detect statistically significant correlations between voxels. The two longitudinal samples of this study were used to confirm and replicate the spatial patterns of pathology propagation predicted at the cross-sectional level. For the longitudinal sample, we included all data available to us with two-years of follow up in both, tau and amyloid, PET modalities.

2. Data exclusions

Describe any data exclusions.

None of the individual subjects were excluded from the analysis. Our processing pipeline also included an outlier detection approach based on the assessment of normally distributed values of each voxel within our sample to ensure that only voxels with a normal continuum range of PET values were entered in the regression analysis. Supplementary Figure 1 shows our results of pathology propagation of tau and Aβ with and without removing outliers from the processing pipeline.

3. Replication

Describe the measures taken to verify the reproducibility of the experimental findings.

To asses the robustness and reproducibility of our findings, we used a graph theory approach to predict at the cross-sectional level, and confirm and replicate at the longitudinal level, the pathways in which cortical tau and Aβ spread and accumulate, using Flortaucipir- and PiB-PET imaging in several groups of adult participants from the Harvard Aging Brain Study. Moreover, we used an independent longitudinal sample to replicate our main findings. Replication attempts were successful.

4. Randomization

Describe how samples/organisms/participants were allocated into experimental groups.

The main findings of our study are based on cognitively normal elderly individuals without any experimental categorization. Thus, we believe this point does not apply in our case. In a secondary analysis, we compared a group of elderly controls and Alzheimer's disease participants based on well-established clinical criteria.

5. Blinding

Describe whether the investigators were blinded to group allocation during data collection and/or analysis.

All data was acquired as part of the Harvard Aging Brain Study (HABS). The HABS protocol involves blinded subject identifiers for study participants during data sharing and analysis. As our study is based on cognitively normal elderly individuals without any group allocation/ segregation, we believe this point does not apply in our case.

Note: all in vivo studies must report how sample size was determined and whether blinding and randomization were used.

6. Statistical parameters

For all figures and tables that use statistical methods, confirm that the following items are present in relevant figure legends (or in the Methods section if additional space is needed).

n/a	Confirmed
☐	☒ The exact sample size (*n*) for each experimental group/condition, given as a discrete number and unit of measurement (animals, litters, cultures, etc.)
☐	☒ A description of how samples were collected, noting whether measurements were taken from distinct samples or whether the same sample was measured repeatedly
☐	☒ A statement indicating how many times each experiment was replicated
☐	☒ The statistical test(s) used and whether they are one- or two-sided *Only common tests should be described solely by name; describe more complex techniques in the Methods section.*
☐	☒ A description of any assumptions or corrections, such as an adjustment for multiple comparisons
☐	☒ Test values indicating whether an effect is present *Provide confidence intervals or give results of significance tests (e.g. P values) as exact values whenever appropriate and with effect sizes noted.*
☐	☒ A clear description of statistics including central tendency (e.g. median, mean) and variation (e.g. standard deviation, interquartile range)
☐	☒ Clearly defined error bars in all relevant figure captions (with explicit mention of central tendency and variation)

See the web collection on statistics for biologists for further resources and guidance.

Software

Policy information about availability of computer code

7. Software

Describe the software used to analyze the data in this study.

We used Matlab v8.0 (Mathworks Inc., Natick, MA) for imaging, graph theory and statistical analyses. We used SPM12 (Wellcome Centre for Human Neuroimaging, University College London, London, UK, http://www.fil.ion.ucl.ac.uk/spm), and its VBM8 toolbox, for structural imaging processing. We used Caret v5 software for imaging surface projections. We used Gene Ontology (www.geneontology.org/), Genemania v3.4 (http://www.genemania.org) and Cytoscape v3.4 (www.cytoscape.org) for genetic annotation and interaction analyses.

For manuscripts utilizing custom algorithms or software that are central to the paper but not yet described in the published literature, software must be made available to editors and reviewers upon request. We strongly encourage code deposition in a community repository (e.g. GitHub). *Nature Methods* guidance for providing algorithms and software for publication provides further information on this topic.

Materials and reagents

Policy information about availability of materials

8. Materials availability

Indicate whether there are restrictions on availability of unique materials or if these materials are only available for distribution by a third party.

n/a

9. Antibodies

Describe the antibodies used and how they were validated for use in the system under study (i.e. assay and species).

n/a

10. Eukaryotic cell lines

a. State the source of each eukaryotic cell line used.

n/a

b. Describe the method of cell line authentication used.

n/a

c. Report whether the cell lines were tested for mycoplasma contamination.

n/a

d. If any of the cell lines used are listed in the database of commonly misidentified cell lines maintained by ICLAC, provide a scientific rationale for their use.

n/a

Animals and human research participants

Policy information about studies involving animals; when reporting animal research, follow the ARRIVE guidelines

11. Description of research animals

Provide all relevant details on animals and/or animal-derived materials used in the study.

n/a

Policy information about studies involving human research participants

12. Description of human research participants

Describe the covariate-relevant population characteristics of the human research participants.

We included 88 clinically normal participants from the HABS ([mean age (SD): 72.24 (11.63), M/F: 43/45]; see Supplementary Table 1 for detailed demographics and clinical characteristics), out of which 19 also had a two-year follow-up assessment [mean age (SD): 75.63 (5.95), M/F: 11/8]. Apart from the main longitudinal sample, we included an additional longitudinal sample of 24 HABS individuals [mean age (SD): 76.09 (5.66), M/F: 9/15] for validation and replication of our propagation method and findings. This replication sample was also used to investigate partial volume correction (PVC) effects on PET images. We also included 19 participants previously classified as cognitively impaired by memory clinics of Harvard School of Medicine-affiliated hospitals, including diagnoses of mild cognitive impairment (MCI) or AD dementia [mean age (SD): 67.45 (9.12), M/F: 14/5; mean CDR-SB (SD): 3.82 (2.91); mean Mini-Mental State Examination (MMSE): 24.47 (4.95)]. As part of HABS, participants undergo multiple neuroimaging sessions, APOE genotyping, and an annual neuropsychological testing that includes the Preclinical Alzheimer's Cognitive Composite (PACC). The PACC combines Logical Memory Delayed Recall, MMSE Total score, Wechsler Adult Intelligence Scale-Revised Digit Symbol coding, and the Free and Cued Selective Reminding Test. Direct genotyping of APOE rs7412 and rs429358 is performed at the Harvard Neurodiscovery Center to derive APOE haplotypes. Participants are originally included if they have a score of 0 on the Clinical Dementia Rating (CDR) scale, a MMSE score ≥ 25, and if they perform within education-adjusted norms on the Logical Memory delayed recall test (>10 for ≥ 16 years of education, >6 for 8-15 years of education and >4 for <8 years of education). All participants undergo at least one comprehensive medical and neurological evaluation, and must not have any medical or neurological disorders at enrollment that could contribute to their cognitive abilities. Presence of clinical depression (Geriatric Depression Scale above 11/30) or other psychiatric illnesses, history of alcoholism, drug abuse, head trauma, or a family history of autosomal dominant AD dementia were exclusionary criteria. All participants took part in the study using protocols and informed consent procedures approved by the Partners Human Research Committee at the Massachusetts General Hospital.